Particle Filtration in Sandstone Cores: Application of a Chemical Shift Imaging Technique

Christian Straley, Dan Rossini, and Lawrence M. Schwartz

Schlumberger-Doll Research
Old Quarry Road, Ridgefield, CT 06877-4108

and

Michael E. Stromski, Mirko Hrovat, and Samuel Patz

Radiology Department, Brigham and Womens Hospital
Harvard Medical School, Boston, MA 02115

Abstract

Recent developments have led to increased interest in the application of borehole nuclear magnetic resonance (NMR) as a probe of petrophysical properties. Of particular importance in this connection is the measurement of the longitudinal relaxation time, T_1. As T_1 is, to a large extent, controlled by the effective pore surface area, its value may be strongly influenced by the invasion of submicron-sized clay particles found in drilling muds. We have undertaken a quantitative study of this effect by the application of novel magnetic resonance imaging (MRI) techniques. The resolution of conventional readout gradient MRI is limited in sandstone cores by the presence of internal field gradients associated with either paramagnetic impurities or the natural susceptibility contrast between the predominantly quartz matrix and the pore fluid. This problem can be overcome by the application of a phase encode (i.e. chemical shift) imaging sequence. The utility of this technique will be illustrated by a study of the effect of bentonite invasion on T_1 values in Berea sandstones. Our experimental results indicate that the extent to which T_1 values are affected by particulate invasion depends on several characteristics of the drilling mud. In the case of spud muds (i.e. simple bentonite slurries) we see a region deep within the core where T_1 values are significantly reduced due to an initial *spurt* of clay particles. In better formulated muds this effect is greatly reduced. Our imaging studies are supported by measurements made using a laboratory "inside-out" NMR spectrometer which measures a T_1 value at single depth (roughly 2 *cm*) below the inflow core end.

1 Introduction

In the last few years a great deal of work has been done on the application of magnetic resonance tomography to the study of porous media.[1-7] Much of this work has focused on the description of the naturally heterogeneous structure of reservoir sandstones and carbonates. In the present paper we will be concerned with the application of MRI to the study of inhomogeneities introduced by the invasion of fine grained particles found in drilling fluids and, in particular, with the influence of these particles on the longitudinal relaxation time, T_1. There are many studies which empirically show that the T_1 value in water saturated sandstones can be related to other physical properties of practical importance;[1,8-13] such as the permeability to viscous fluid flow and the irreducible water fraction. If these empirical relations are to be applied to borehole data, we must be confident that the T_1 measurements have not been compromised by the invasion of clay fines suspended in the drilling muds. This problem is of particular importance in light of recent advances in the area of borehole NMR measurement technology.[14,15] Although we are using imaging techniques, it should be emphasized that the objectives of this study are *quantitative*; we want a high resolution mapping of the spatial variation of T_1 in sandstone and carbonate rocks.

2 Experimental Procedure

2.1 The Choice of Imaging Technique

Our measurements were performed on a 60 *cm* bore 1.5 *T* imaging system. The system is equipped with actively shielded gradient coils capable of gradient strengths up to 2 *G/cm*. We are dealing with cylindrical sandstone cores (length, 7.62 *cm*; diameter, 5.08 *cm*) and our aim is to measure the effective T_1 value in circular slices oriented normal to the core axis. The standard technique by which one might try to obtain such a projection is to perform a simple spin echo experiment with a readout gradient applied parallel to the core axis [Figure 1a]. A problem arises with this technique, however, when the natural linewidth of the sample, $\Delta\omega_S$, (in the absence of any applied gradient) is comparable to the frequency shift, $\Delta\omega_g$, between adjacent points in the projection induced by the applied gradient.[16] If Δz is the desired axial resolution and G_z is the magnitude of the readout gradient, then

$$\Delta\omega_g = \gamma G_z \Delta z \ , \tag{1}$$

where γ is the proton gyromagnetic ratio. To illustrate the problem, we show schematically in Figure 1b the spectrum of the sample at three axial positions, z_1, $z_2 = z_1 + \Delta z$, and $z_3 = z_2 + \Delta z$. With $G_z = G_1$, $\Delta\omega_S > \Delta\omega_g$, and some of the spectral components from the material located at z_1 and z_3 will have the same frequency as the material at z_2. Certainly, under these conditions contributions from z_1, z_2, and z_3 cannot be resolved. On the other hand, for $G_z = G_2$, we have $\Delta\omega_S < \Delta\omega_g$, and the material at z_1 and z_3 no longer has frequency components that overlap the z_2 spectrum.

To estimate the values of G_z required for 1 mm resolution, we measured the proton spectrum from a typical Berea sandstone core at a field strength of 1.5 T. This sample has a porosity, ϕ, of roughly 20.1 %, a permeability, k, of about 130 md, and an iron concentration of 0.20 %; at a Larmor frequency of 10 MHz, the measured T_1 value was 300 ms. The magnitude spectrum shown in Figure 2 is basically a single broad line with a full width at half maximum of 7200 Hz. Setting $\Delta\omega_S = (2\pi) \times 7200$, the gradient strength required for 1 mm resolution is determined by the requirement

$$\Delta\omega_g = \gamma G \Delta z > \Delta\omega_S \; ; \; \text{or} \; \; G > \frac{\Delta\omega_S}{\gamma \Delta z} \approx 16.9 \, G/cm \; . \tag{2}$$

This is roughly an order of magnitude greater than the gradients available on most magnetic resonance imaging machines. Using the maximum gradient strength available on our equipment, 2 G/cm, resolution would be about 8.5 mm. Not only is the resolution along the readout gradient direction compromised, but for similar reasons, we are unable to excite thin slices using selective rf pulses in conjunction with a slice selective gradient.

To solve these problems,[17] we employed the chemical shift (phase encode) method shown in Figure 3.[5,18–20] In the present case, where we have only a single broad line, we are not interested in resolving multiple chemical species. Instead, our aim is to separate the phase precession (and the associated dephasing) due to the internal magnetic field inhomogeneities which are responsible for the natural linewidth from the dephasing caused by the position encoding gradient. Thus the *internal* linewidth has no bearing on the resolution in the z direction. Clearly, the other spatial directions, x and y, can be phase encoded as well if one wants to resolve information in those dimensions.

Let us make clear how the phase encode method separates the two contributions to phase precession. Note, from Figure 3, that the phase encoding gradient pulse (which provides the z resolution) is completed before the spin echo signal is acquired. Thus, the encode gradient (whose duration we denote as t_{pe}) determines only the phase, ϕ_o, which a given spin has at the beginning of the acquisition interval

$$\phi_o(z) = \gamma G_z t_{pe} z \equiv k_z z \; , \tag{3}$$

Consider a spin in slice z; if t measures the elapsed time during data acquisition, the net phase change during this interval can be written as a sum of two terms

$$\delta\phi_{net} = \phi_o(z) + \delta\phi_i(t) \equiv k_z z + \omega_i t \; . \tag{4}$$

Here $\delta\phi_i(t)$ is the phase change associated with the *internal* field inhomogeneities. [At each slice location, z, there are, of course, a distribution of ω_i values.] During the data acquisition interval, the two components of transverse magnetization in the rotating reference frame (apart from their T_2 dependence) may then be written as

$$M_1 = M_o sin(k_z z + \omega_i t) \; ; \quad M_2 = M_o cos(k_z z + \omega_i t) \; . \tag{5}$$

Now, for each value of the initial phase ϕ_o (i.e. for each k_z) the acquired time dependent signal is Fourier transformed to give a spectrum in ω_i. As indicated in Figure 3, the experiment is then repeated at different gradient strengths to obtain a set of ω_i spectra, each labeled by a different value of k_z. Next, for each ω_i, a second Fourier transform is performed on the k_z data to resolve the z dependence of the signal. The resulting two dimensional data set then contains an ω_i spectrum for each z value and there is no mixing of the two contributions in Eq. (4).

Another important reason to use the chemical shift method to image sandstones is because shorter values of T_E can be obtained. If the value of T_E is too long, a significant fraction of the pore fluid will not be observed because its T_2 value is so short. For example, in our work with the readout gradient method, the value of T_E was 4.5 ms and we estimated that only about 40% of the pore fluid contributed to the signal. With the phase encoding method we were able to reduce T_E to roughly 2 ms and we estimate that about 70% of the water contributed. Note, that with the readout gradient technique, it is much more difficult to reduce T_E because this method requires an additional dephasing gradient pulse between the 90 and 180 degree rf pulses. [The inherent gradient switching time is roughly 1 ms.]

A final concern associated with the large linewidths discussed above was that the 90 and 180 degree pulses might not have sufficient bandwidth to excite the entire spectral width of our sample. To insure that this would not be a problem, a special solenoidal coil was constructed to guarantee especially short rf pulses. Typical pulse lengths were 12 and 24 μs for the 90 and 180 degree pulses respectively.

It is interesting to ask what limits the resolution of our measurements along the z axis. There are two limiting factors: a theoretical bound associated with diffusion which would act even if infinitely strong gradients were available, and a Nyquist limit associated with our particular equipment. The Nyquist limit of the chemical shift method is

$$\Delta z_N = \frac{1}{2\gamma t_{pe}\{G_z\}_{max}} . \tag{6}$$

If we take $(T_E/2) \approx 1.1\, ms$ as a maximum value of t_{pe}, and $\{G_z\}_{max} = 2\, G/cm$, then $\Delta z_N \approx 0.053 mm$. The fundamental limit, Δz_D, due to diffusion can be estimated by calculating the distance traveled along the z direction by a diffusing water molecule during the time interval T_E. At room temperature,

$$\Delta z_D = [2DT_E]^{1/2} \approx 0.003\, mm \ . \tag{7}$$

Clearly, our hardware is the limiting factor in determining the spatial resolution of the measurements.

To measure T_1, an inversion pulse is applied at a time T_I before the chemical shift excitation (as shown in Figure 3) and the signal is then measured as a function of T_I. Different phases of the pulse sequence were averaged to cancel out unwanted components of the signal. A total of four averages were acquired, two for the stimulated echo which results from the 180-90-180 pulse sequence and two for the free induction decay associated with the final 180 pulse. Twenty one values of T_I, ranging from 5.0 ms to 4177 ms, were employed. The recovery time between excitation sequences, T_R,

was set to 5 s. In this way, longitudinal relaxation curves could be obtained with millimeter resolution along the core axis. At each z position the measured inversion recovery curve was fit to a stretched exponential form[10]

$$M(z,t) = M_o(z)\exp[-(t/T_1)^{\alpha}] \ , \tag{8}$$

from which we derived a T_1 value. Here the parameter $\alpha \leq 1$ allows us to model the fact that the decay of magnetization in porous media is generally non-exponential in character. Physically, this behavior is associated with the wide range of pore sizes found in most systems of practical interest.

2.2 Example of Phase Encode Spectroscopy

To illustrate the kind of information available with the chemical shift method, let us consider a phantom core comprised of adjacent Berea 100 and Berea 600 sections. Typical imaging parameters used were: phase encoding time, $t_{pe} = 0.8\,ms$, echo time, $T_E = 2.2\,ms$, $\{G_z\}_{max} = 1.6\,G/cm$, and a total of 256 phase encoding steps. With these parameters, the field of view along z was 23.5 cm and $\Delta z = 0.093\ cm$.

In Figure 4, results for three values of the inversion parameter, T_I, are presented. The lower panels show images in which the horizontal direction corresponds to the axial position, z, and the chemical shift spectrum at each z is represented by a grey scale coding along the vertical (frequency) axis. In the upper panels the same data is presented in a three dimensional grid display. We believe that the curvature seen on Berea 600 side of the sample is a finite size effect analogous to fringing fields in capacitors. The configuration of the sample in the magnet is such that the static magnetic field is *normal* to the core axis. If the core diameter were very small compared to its length, the induced internal magnetic fields (which, on the average, are aligned with the static field) would be nearly uniform along the core axis. However, because the core diameter is large, the induced fields near its ends are relatively weak and the internal frequency spectra are shifted relative to the spectra associated with the middle of the core. Because the porosity of the Berea 600 plug is larger than that of the Berea 100 plug, this effect is seen most clearly at the left side of the sample.

In the upper panel of Figure 5 we show the corresponding projections, obtained by integrating the signal over frequency (i.e. over the chemical shift axis). Here, as in Figure 4b, one sees that the transition from negative to positive values takes place more quickly on the Berea 100 side of the sample. [Thus, for $T_I = 396\ ms$, positive values are obtained on the Berea 100 side of the core while the values on the Berea 600 side are still negative.] When all twenty one inversion times are taken into account, the resulting stretched exponential fits yield the T_1 values plotted in the lower panel of Figure 5. Here we see that, despite the structure seen in Figure 4 and the upper panel of Figure 5, the lifetime distributions are quite uniform within the two halfs of the phantom. To interpret the lifetimes of 475 ms and 700 ms (indicated by the arrows) let us examine the full T_1 distributions[12] obtained for these rocks [Figure 6]. While the spectra for both Berea 100 and Berea 600 contain contributions spread

over more than three decades along the T_1 axis, it is clear that the lifetimes estimated from Figure 5 correspond well to the peaks at the upper portion of both spectra. Physically, these peaks are associated with the larger pores in each sample. This correspondence is not surprising because, as noted above, our imaging measurements are limited to T_E values on the order of 2 ms and are thus insensitive to fluids in the smallest pores.

3 Particle Filtration Experiments

Our mud injection experiments were carried out using a modified Baroid OFI mud press. The cores were jacketed with an epoxy coating to eliminate leakage around the sides and 100 ml of drilling fluid was placed in the press chamber above the core. The injection experiments were then run at constant applied pressure and were continued until up to one pore volume of fluid was collected below the out-flow core end. Before injection, the cores were saturated with 0.20 Ωm brine and subjected to two sets of NMR measurements. Both ends of each core sample were examined using a laboratory version of a recently developed "inside-out" spectrometer.[14] The depth of investigation of this instrument is approximately 2.0 cm and the measurements are processed to give values of T_1 and α. Selected cores were then imaged (as described above) to obtain T_1 profiles over the entire core length. After injection with drilling mud, the measurements made before invasion were repeated to monitor the changes in T_1 caused by particulate invasion.

3.1 Choice of Drilling Muds

The properties of the drilling muds used in this study are summarized in Table 1. Included in each case are the values of T_1 and α for both the mud and the mud filtrate (obtained by passing the mud through Baroid 725 filter paper). While the values of T_1 for the muds are typically quite short, in most cases the filtrate T_1 is between two and three seconds. Exceptions are the lignosulfonate and KCL/polymer muds where the T_1 values are 500 ms or less. Our invasion studies employed only those muds for which the filtrate T_1 values were greater than 2 seconds. For these systems, the short lifetimes in the original mud are due to physical, rather than chemical effects (i.e. to excess surface area associated with clay fines). In such muds one might reasonably expect the motion of the fluid through the porous rock to mimic its passage through the filter paper, i.e. to "clean-up" the fluid and return the T_1 values to roughly those characteristic of bulk water.

3.2 Measurements with "Inside-Out" NMR Spectrometer

The results of our measurements with the remote laboratory NMR system are summarized in Table 2. Here we see that in "spud muds" (i.e. simple bentonite slurries)

one finds a significant reduction of T_1 at the 2 *cm* depth probed by this spectrometer. As expected, this reduction is most dramatic in the higher permeability rocks (e.g. a 35% reduction in Berea 100 compared to a 65% reduction in Berea 600). Interestingly, we note that there is very little T_1 depression near the end of the core opposite the invasion. Thus, it appears that even when a full pore volume of spud mud entered the sample, the bentonite fines were eventually filtered by the rock, and only relatively clean fluid penetrated deeply into the core. [If less than a pore volume was involved in the flow, then, assuming that fluid dispersion was not significant, no change in T_1 near the outflow end would be expected.]

We emphasize that spud muds provide a rather unrealistic "worst case" picture of particle invasion. It is clear from Table 2 that the depression of T_1 values is not significant when the mud contains polymer gels that enhance the formation of filter-cake at the in-flow end of the core. In this case the effect is often as small as a few percent and we may conclude that the bentonite particles are essentially removed from the suspension at a depth of 2 *cm*.

3.3 Imaging Measurements

The results of our imaging studies of bentonite invasion are summarized in Figures 7 through 9. Figures 7 and 8 involve the invasion of spud muds into Clashach and Berea sandstones. The Clashach sample is of interest because the imaging and remote NMR measurements both show that there is considerable variation of T_1 within the original core. Presumably, this variation reflects changes in the mean pore size along the core axis. After invading with mud from the short T_1 end, both the imaging and remote NMR measurements indicate a substantial T_1 reduction (roughly 50%). The profile in Figure 7 indicates that this depression covers at least the first inch below the in-flow end of the core. It should be noted that the T_1 values seen by the imaging measurements are considerably longer than those obtained with the remote NMR spectrometer. Once again, this reflects the fact that the longer echo times required in MRI experiments limit us to seeing only the water in the larger pores.

Consider next the results for Berea 100 and Berea 600 shown in Figure 8. Here we see a well defined minimum in the T_1 profile which appears to be due to an initial spurt of bentonite particles. Because the spud mud is ineffective in building a filter-cake in the injection process, the bentonite fines that first enter the core can penetrate quite deeply. In the present series of experiments the flow was interrupted after roughly half a pore volume of fluid had entered the core. While this interruption certainly limits the depth of bentonite penetration, we emphasize that, by the time a pore volume of filtrate had been collected below the sample, a substantial filter-cake had built up at the in-flow end, and the flow rate was, in fact, quite low. Thus, we believe that even if we had continued to apply pressure, the depth of particle penetration would not have increased significantly. In this connection let us make two observations. First, that the penetration appears to be deeper in the higher permeability core sample (Berea 600). This is reasonable on physical grounds, because the fines are expected to flow more easily into the larger pore network. Second, if instead of allowing the filter-cake to grow with time, we had been continuously removing the cake (as might be the case in a borehole environment where the drill constantly scrapes the formation wall)

then the depth of bentonite penetration would be expected to increase significantly. Experiments designed to check this point are now in progress.

Finally, we consider in Figure 9 an invasion experiment based on a 1.3 gm/cc barite weighted mud. Here, the T_1 values show a weak minimum centered roughly 4.5 cm into the core. The fact that the T_1 depression is considerably weaker here than in either Figures 7 or 8 is, of course, consistent with the results discussed in connection with Table 2. The enhanced filter cake formation has limited the number of bentonite particles flowing into the core, although the depth of penetration for those that do enter is still quite significant. Further studies with a wider range of drilling muds are now in progress; we are especially interested in the role of weighting agents (e.g. barite) in limiting the penetration of bentonite fines.

4 Conclusions

In the present manuscript we have presented the preliminary results of our study of the influence of drilling mud invasion on the longitudinal NMR lifetime, T_1. Although our experiments are still in progress, we are, at this point, able to advance several conclusions:

- Phase encode imaging yields high resolution T_1 profiles in sandstone cores even when the natural linewidths of the sample are quite broad (e.g several kHz).

- With simple bentonite slurries (spud mud) particle invasion can be seen clearly and can depress T_1 values several centimeters into the core sample.

- With well constructed (e.g. polymer-gel or Barite weighted) muds the invasion by bentonite fines is suppressed and T_1 values are essentially unaffected past depths on the order of a centimeter.

- Measurements made using MRI and remote NMR spectroscopy are in good qualitative agreement.

5 Acknowledgement

During the course of this work we have benefited from discussions with F. Auzerais, E. Fordham, W. Kenyon, R. Kleinberg, and S. Kostek.

References

1. A useful review of recent work in this field can be found in *Proceedings of the First International Conference on Recent Advances in NMR Applications to Porous Media, November 14-16, 1990, Bologna, Italy*, Magnetic Resonance Imaging, **9**, No. 5 (1991).

2. R. J. Gummerson, C. Hall, W. D. Hoff, R. Hawkes, G. N. Holland, and W. S. Moore, Unsaturated Water Flow Within Porous Materials Observed by NMR Imaging, Nature, **281** 56 (1979).

3. H. Vinegar, X-Ray CT and NMR Imaging of Rocks, J. Petroleum Technology, **38**, 257 (1986).

4. P. Blackband, P. Mansfield, J. R. Barnes, A. D. H. Clague, and S. A. Rice, Discrimination of Crude Oil and Water in Sand and Bore Cores with NMR Imaging, SPE Formation Evaluation, page 31, February, 1986.

5. L. D. Hall and V. Rajanayagam, Thin-Slice Chemical Shift Imaging of Oil and Water in Sandstone Rock at 80 MHz, J. Magnetic Resonance, **74**, 139 (1987).

6. W. A. Edelstein, H. J. Vinegar, P. N. Tutunjian, P. B. Roemer, and O. M. Mueller, NMR Imaging for Core Analysis, SPE 18272, Presented at the 63^{rd} Annual Technical Conference and Exhibition of the Society of Petroleum Engineers, Houston, TX, October, 1988.

7. J. D. Chen, M. M. Dias, S. Patz, and L. M. Schwartz, Magnetic Resonance Imaging of Immiscible-Fluid Displacement in Porous Media, Phys. Rev. Letters **61**, 1489 (1988).

8. A. Timur, Pulsed Nuclear Magnetic Resonance Studies of Porosity, Movable Fluid and Permeability of Sandstones, J. Pet. Tech., **21**, 775, June (1969); Producible Porosity and Permeability of Sandstones Investigated through Nuclear Magnetic Resonsnace Principles, The Log Analyst, **10**, No. 1, 3 (1969); An Investigation of of Permeability, Porosity, and Residual Water Saturation Relationships, Trans. 9^{th} Annual SPWLA Symposium, Paper K (1968).

9. J. D. Loren and J. D. Robinson, Relations Between Pore Size, Fluid and Matrix Properties, and NML Measurements, Soc. Pet. Eng. Journal, **10**, 268, Sept. 1970.

10. W. E. Kenyon, P. Day, C. Straley, and J. Willemsen, A Three Part Study of NMR Longitudinal Relaxation Properties of Water Saturated Sandstones, SPE Formation Evaluation **3**, 622, 1988.

11. J. R. Banavar and L. M. Schwartz, Magnetic Resonance as a Probe of Permeability in Porous Media, Phys. Rev. Letters, **58**, 1411 (1987); J. R. Banavar and L. M. Schwartz, Probing Porous Media with Nuclear Magnetic Resonance, *Molecular Dynamics in Restricted Geometries* Edited by J. Klafter and J. M. Drake, (John Wiley & Sons, 1989) Page 273.

12. W. E. Kenyon, J. J. Howard, A. Sezginer, C. Straley, A. Meteson, K. Horkowitz, and R. Ehrlich, Pore-Size Distribution and NMR in Microporous Cherty Sandstones, Trans. 30^{th} Annual SPWLA Symposium, Paper LL (1989).

13. C. Straley, C. E. Moriss, W. E. Kenyon, and J. J. Howard, NMR in Partially Saturated Rocks: Laboratory Insights on Free Fluid Index and Comparison with Borehole Logs Trans. 32^{nd} Annual SPWLA Symposium, Paper CC (1991).

14. A Novel NMR Apparatus for Investigating an External Sample, R. Kleinberg, A. Sezginer, D. Griffin, and M. Fukuhara, Magn. Resonance, April, 1992.

15. The MRIL in Conoco 33-1: An Investigation of a New Magnetic Resonance Imaging Log, G. R. Coates, M. Miller, M. Gillen, and G. Henderson, Transactions, 32^{nd} Logging Symposium, June 16, 1991, Midland, TX, Paper DD.

16. While the linewidths described here are typical of sandstones, there are rocks that exhibit much sharper lines and, for such rocks, the readout gradient approach works quite well. See E. J. Fordham, M. A. Horsfield, M. A. Hall, C. Hall. L. D. Hall, Low Contrast Secondary Imbibition in Long Rock Cores, Magn. Resonance Imaging, **9**, 803 (1991).

17. Application of Single Species Chemical Shift Imaging to Sandstone Cores, S. Patz, M. Stromski, M. Hrovat, C. Straley, and L. Schwartz, Magn. Resonance Imaging, **9**, 797 (1991).

18. J. C. Haselgrove, V. H. Subramanian, L. S. Leigh, L. Gyulai and B. Chance, In Vivo One-Dimensional Imaging of Phosphorous Metabolites by Phosphorous-31 Nuclear Magnetic Resonance, Science, **220**, 1170 (1983).

19. T. R. Brown, B. M. Kincaid, and K. Ugurbil, NMR Chemical Shift Imaging in Three Dimensions, Proceedings of the National Academy of Sciences, USA, **79**, 3523 (1982).

20. A. A. Maudsley, S. K. Hilal, W. H. Perman, and H. E. Simon, Spatially Resolved High Resolution Spectroscopy by "Four Dimensional" NMR, J. Magnetic Resonance, **51**, 147 (1983).

Figure Captions

Figure 1. (a) Schematic representation of rf pulse and applied gradient sequence for the readout gradient technique. An initial inversion pulse, at time T_I before the spin echo sequence, is also shown. (b) The corresponding signal acquisition is pictured for relatively weak and strong applied gradients.

Figure 2. Proton magnitude spectrum from Berea sandstone measured at a field strength of 1.5 T. [Absolute position of frequency axis is arbitrary.]

Figure 3. Schematic representation of rf pulse and applied gradient sequence for the chemical shift technique. As in Figure 1, an inversion pulse is indicated.

Figure 4. Single species chemical shift core images of a Berea 600-100 phantom taken with $T_E = 2.2\ ms$ are shown for three inversion times: (a) $T_I = 5\ ms$, (b) $T_I = 396\ ms$, and (c) $T_I = 41775\ ms$. In the upper panel of each figure the phase encode spectrum is shown as a three dimensional surface, while in the lower panel the same data is displayed as a grey scale image. The Berea 600 data is displayed to the left (front) in the lower (upper) panel.

Figure 5. [Upper Panel] Projections obtained by integrating the data displayed in Figure 4 along the chemical shift axis and [Lower Panel] the stretched exponential fit to T_1 are shown as functions of position along the Berea 600-100 phantom core axis.

Figure 6. T_1 distributions for Berea 100 and Berea 600 are shown with the positions of the arrows taken from the lower panel of Figure 5 marked. The location of the arrows indicates that the lifetimes measured by our imaging techniques are associated with water in the larger pores.

Figure 7. T_1 profiles are shown for a Clashach sandstone core invaded with spud mud.

Figure 8. T_1 profiles are shown for Berea 100 and 600 cores invaded with spud mud.

Figure 9. T_1 profiles are shown for a Berea 100 core invaded with a barite weighted bentonite slurry mud.

About the Authors

Christian Straley has a B.S degree in Chemistry from Washington and Lee University and a M.S. degree from the University of Delaware with an emphasis in Physical Chemistry. He has worked at Schlumberger-Doll Research for ten years and is presently associated with the Interpretation Sciences Department. His primary research interest is the NMR properties of rocks and nuclear magnetism logging; he has also worked on the low frequency electrical properties of fully and partially saturated rocks and on clay properties.

Dan Rossini has a B.S. degree in mechanical engineering from Bridgeport Engineering Institute. He has worked at Schlumberger-Doll Research for eight years and is presently a member of the Interpretation Sciences Department. His research has involved both NMR and acoustic measurements in reservoir rocks.

Lawrence M. Schwartz received his B.S degree from the City College of New York in 1966. He holds M.S. (1967) and Ph.D (1970) degrees from Harvard University. He was a post-doctoral research associate at Harvard until 1972 when he joined the Physics Department at Brandeis University. In 1982 he joined the scientific staff at Schlumberger-Doll research where he now holds the position of Senior Research Scientist. His research interests include the modelling of porous media, transport phenomena, and wave propagation in disordered systems.

Michael E. Stromski received his B.S. (1981) and Ph.D. (1987) degrees in Molecular Biophysics from Yale University. Since 1988 he has worked at Brigham and Womens Hospital of the Harvard Medical School where he is now an Instructor in Radiology. His research deals with the application of NMR imaging to bio-medical and physical problems.

Mirko I. Hrovat received his B.S. degree from Case Western University in 1973 and his Ph.D degree in Physical Chemistry from the University of Texas, Austin 1982. He worked as a post-doctoral fellow (1982-83) Staff Scientist (1983-87) with IBM Instruments in San Jose, CA and Danbury CT. In 1987 he joined the Brigham and Womens Hospital of the Harvard Medical School where he is now an Instructor of Radiology. He also holds a position as a Research Associate at the Massachusetts Institute of Technology. His research deals with the application of NMR imaging to bio-medical and physical problems.

Samuel Patz received his B.S. degree from Emory University in 1971 and his Ph.D degree in Physics from Brandeis University in 1979. He worked as a post-doctoral research associate at Brandeis until 1981 when he joined the Xerox Advanced Products and Technology Department. Since 1983 he has worked at the Brigham and Womens Hospital of the Harvard Medical School where he is now an Assistant Professor of Radiology. His research deals with the application of NMR imaging to bio-medical and physical problems.

Mud Sample Designation	Mud		Filtrate	
	$T_{1,\alpha}$ (ms)	α	$T_{1,\alpha}$ (ms)	α
House Spud	68	0.96	2810	1.00
Barite Weighted Spud (1.3g/cc)	67	0.91	-	-
Barite Weighted Spud (1.8g/cc)	50	0.98	2060	0.98
Mudtech Acrylic Polymer	172	0.99	3208	1.05
Mudtech Acrylic Polymer with Barite	47	0.96	1943	0.99
Mudtech Seawater/Freshwater Gel	95	0.97	3515	1.08
Mudtech Sea/Fresh Gel with Barite	74	0.95	2964	0.99
Mudtech Light Lignosulfonate	23	1.00	130	1.00
Mudtech Seawater Lignosulfonate	22	0.93	351	0.99
Mudtech KCL/Polymer	283	0.95	525	1.02

Table 1. NMR Properties of the ten muds used in this study are summarized. The values of T_1 and α for both the mud and its filtrate were measured using the laboratory *inside-out* spectrometer.

Rock Sample	Invading Mud	T_1 (ms) Before	T_1 (ms) After
Berea D100-3 (inflow)	Spud	229	169
Berea D100-3 (outflow)	-	252	224
Berea 600-1 (inflow)	Spud	478	171
Berea 600-1 (outflow)	-	501	498
Clashach (inflow)	Spud	394	197
Clashach (outflow)	-	541	551
Berea 100	Spud	205	135
Berea 100	Seawater/Freshwater Gel	221	212
Berea 100-Xa	Seawater/Freshwater Gel	124	120
Berea 100-Xb	Barite Sea/Fresh Gel	130	128
Berea 100-Ua	Acrylic Polymer	132	137
Berea 100-Ub	Barite Acrylic Polymer	136	135
Berea 500-Ya	Seawater/Freshwater Gel	465	342
Berea 500-Yb	Acrylic Polymer	450	371

Table 2. A summary of the core invasion measurements made using the *inside-out* spectrometer. In the first six cases the values of T_1 are given for both the inflow and outflow core ends. In the remaining eight case only the values at the inflow end are given. The Berea 100-X and Berea 100-U cores were cut from a different block and generally showed shorter T_1 values than the other Berea 100 cores.

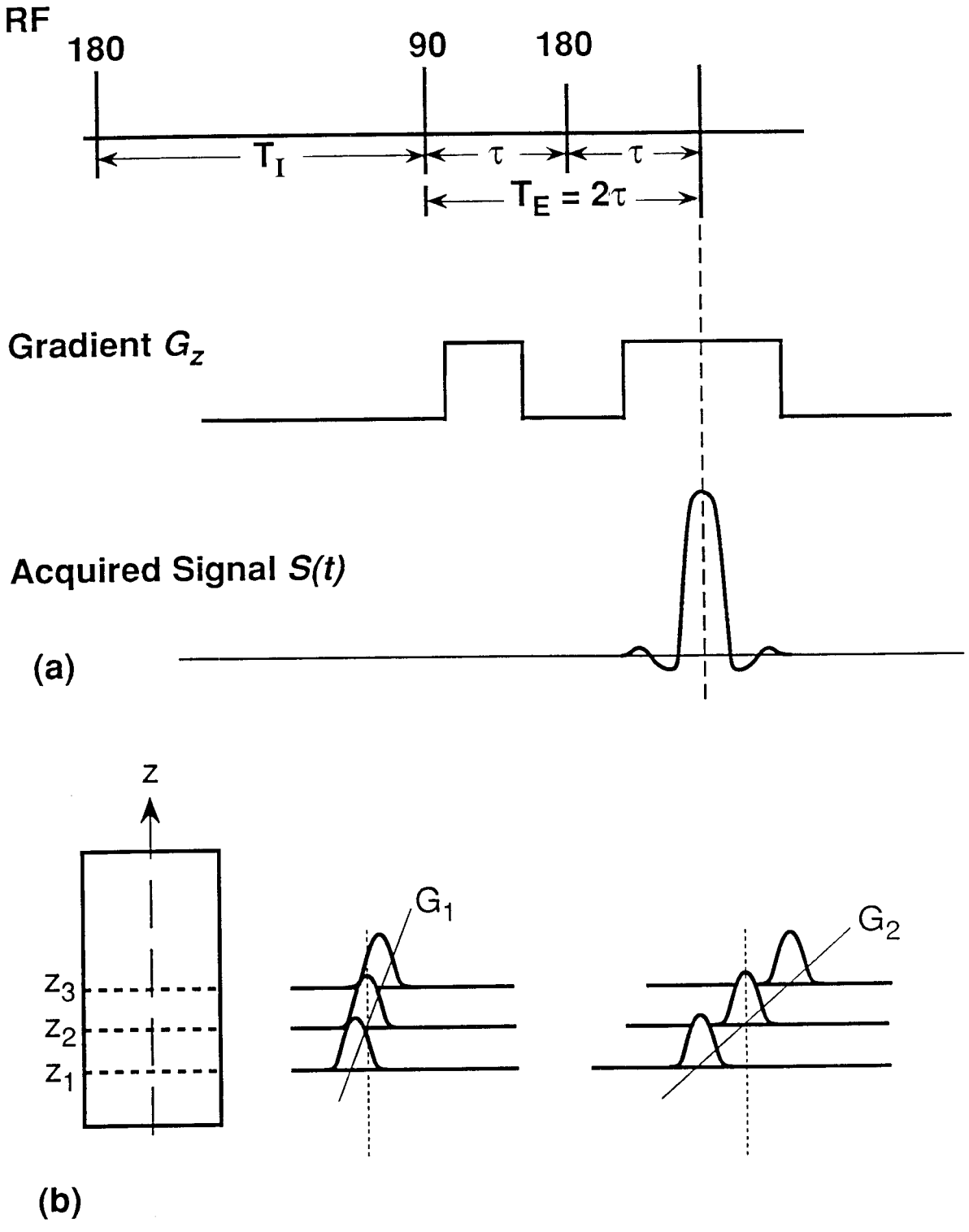

Figure 1. (a) Schematic representation of rf pulse and applied gradient sequence for the readout gradient technique. An initial inversion pulse, at time T_I before the spin echo sequence, is also shown. (b) The corresponding signal acquisition is pictured for relatively weak and strong applied gradients.

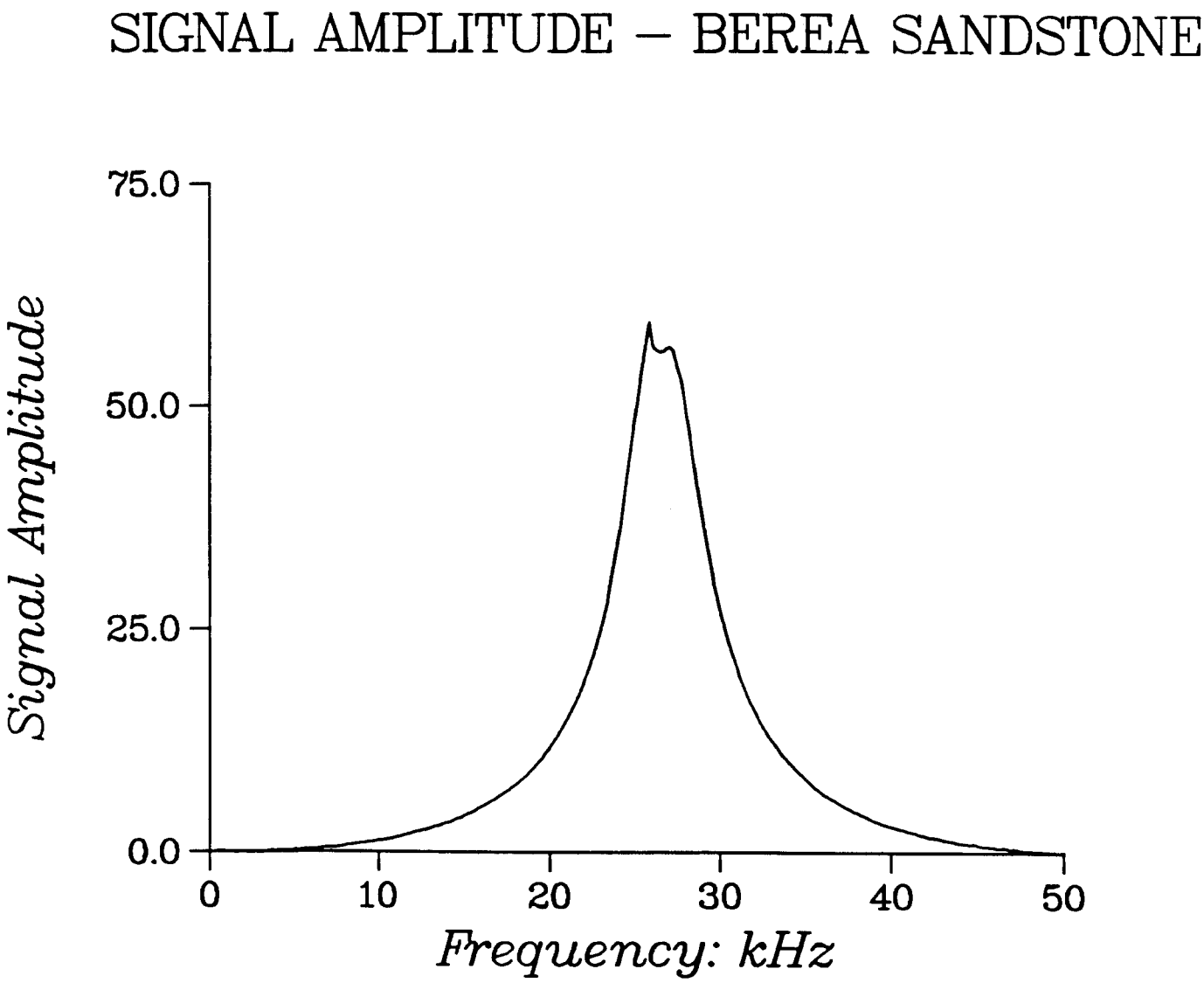

Figure 2. Proton magnitude spectrum from Berea sandstone measured at a field strength of 1.5 T. [Absolute position of frequency axis is arbitrary.]

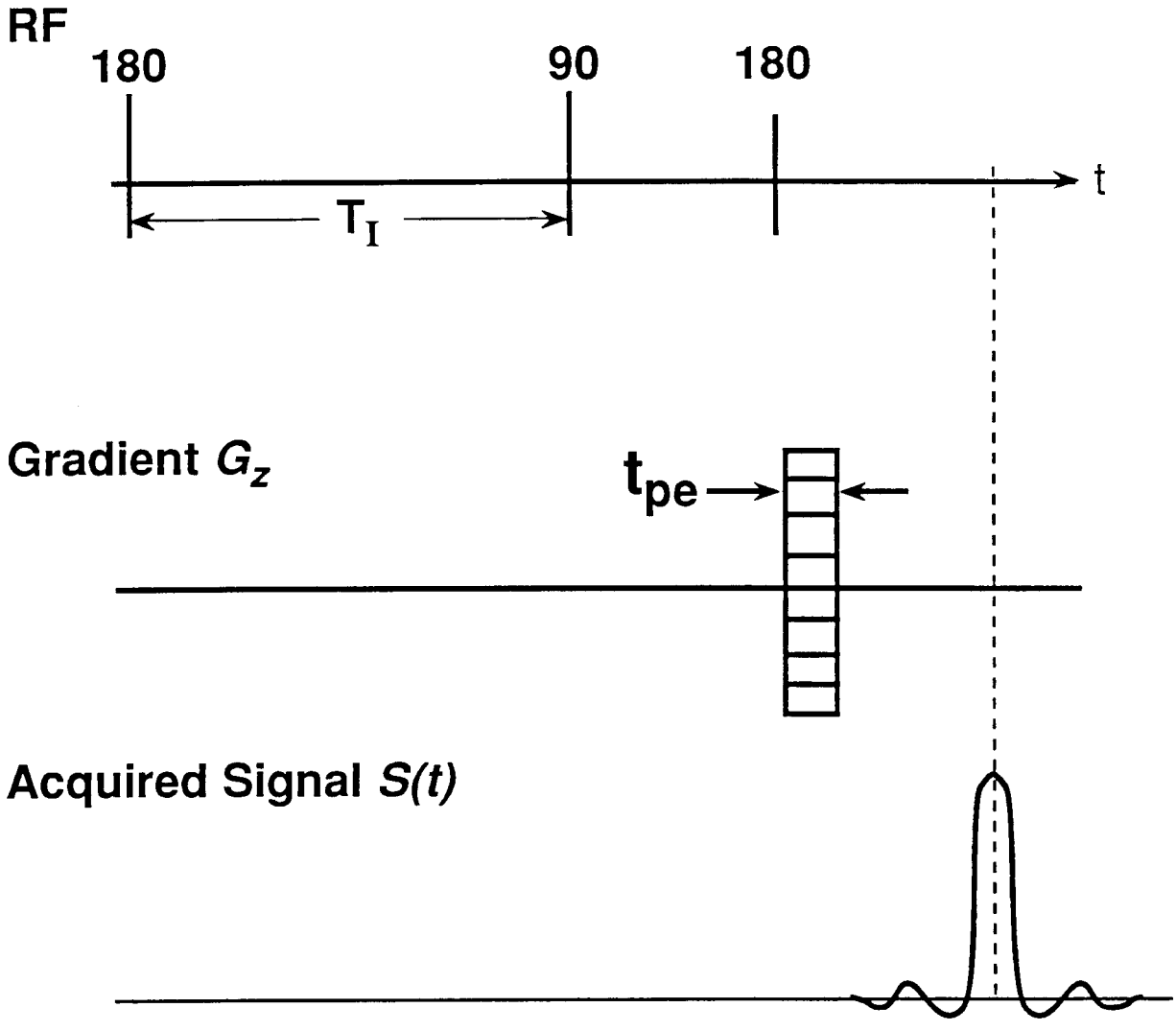

Figure 3. Schematic representation of rf pulse and applied gradient sequence for the chemical shift technique. As in Figure 1, an inversion pulse is indicated.

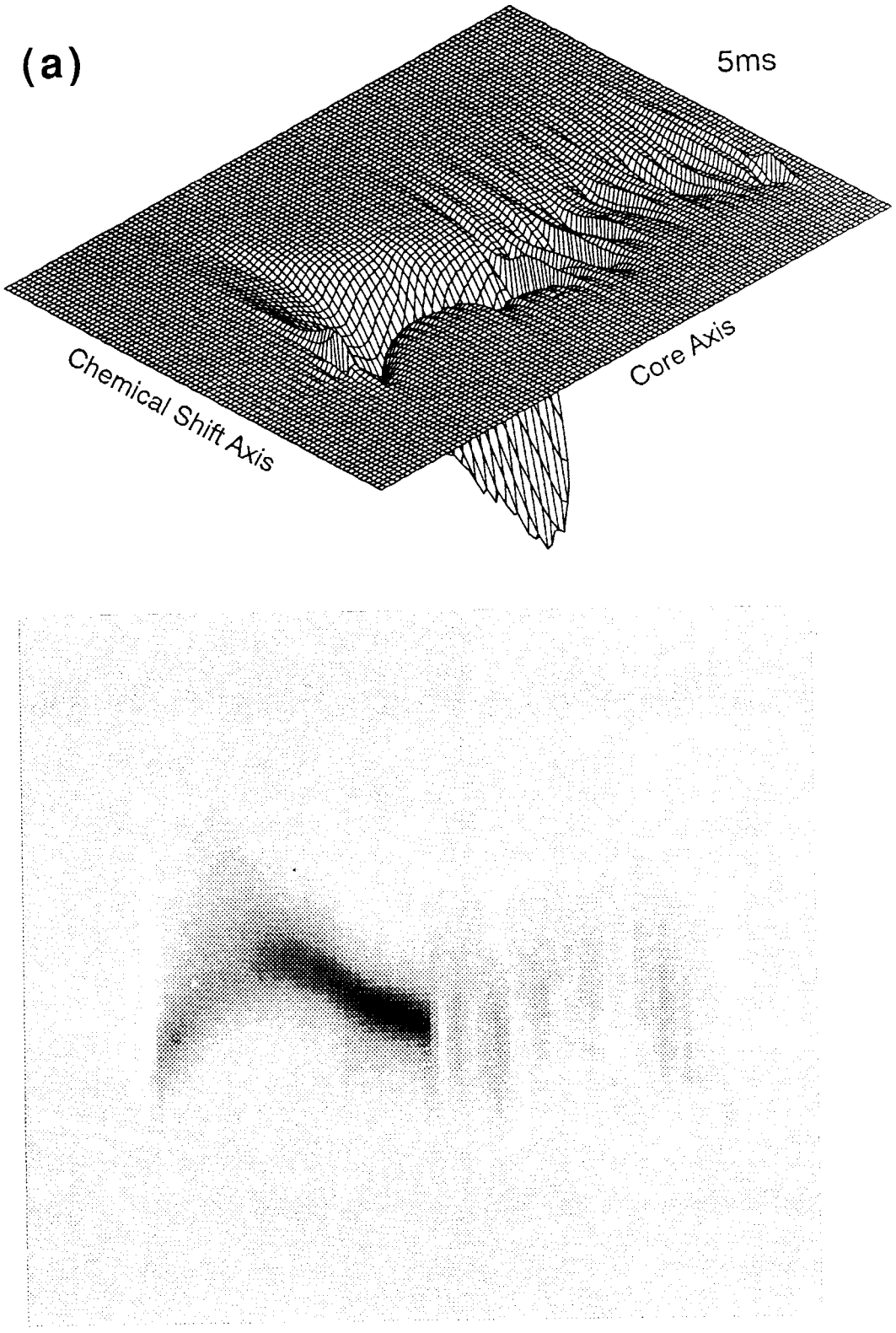

Figure 4. Single species chemical shift core images of a Berea 600-100 phantom taken with $T_E = 2.2\ ms$ are shown for three inversion times: (a) $T_I = 5\ ms$, (b) $T_I = 396\ ms$, and (c) $T_I = 41775\ ms$. In the upper panel of each figure the phase encode spectrum is shown as a three dimensional surface, while in the lower panel the same data is displayed as a grey scale image. The Berea 600 data is displayed to the left (front) in the lower (upper) panel.

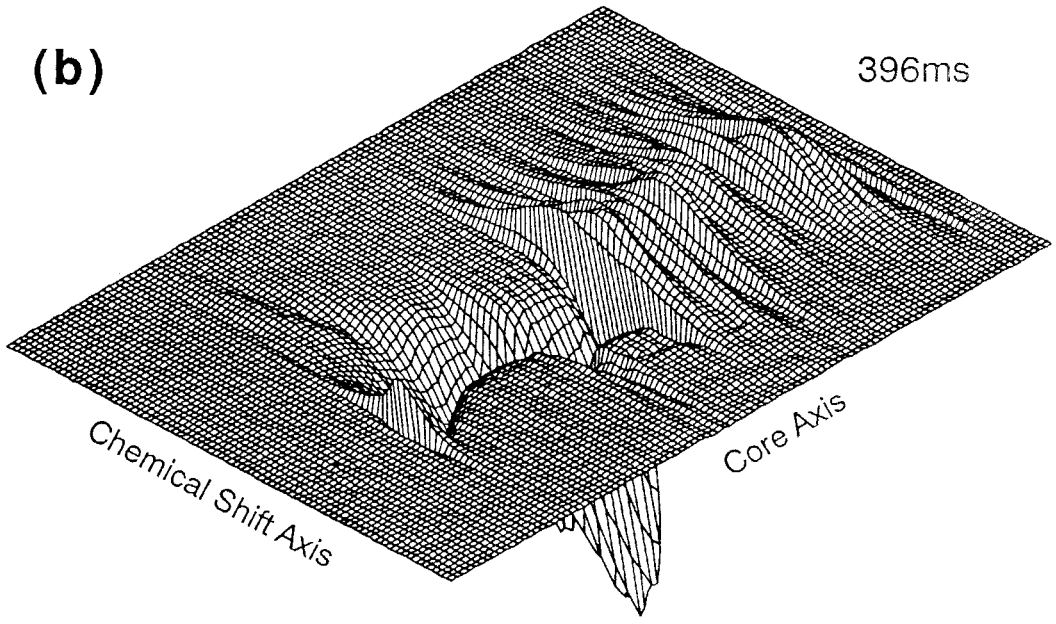
(b)
396ms
Chemical Shift Axis
Core Axis

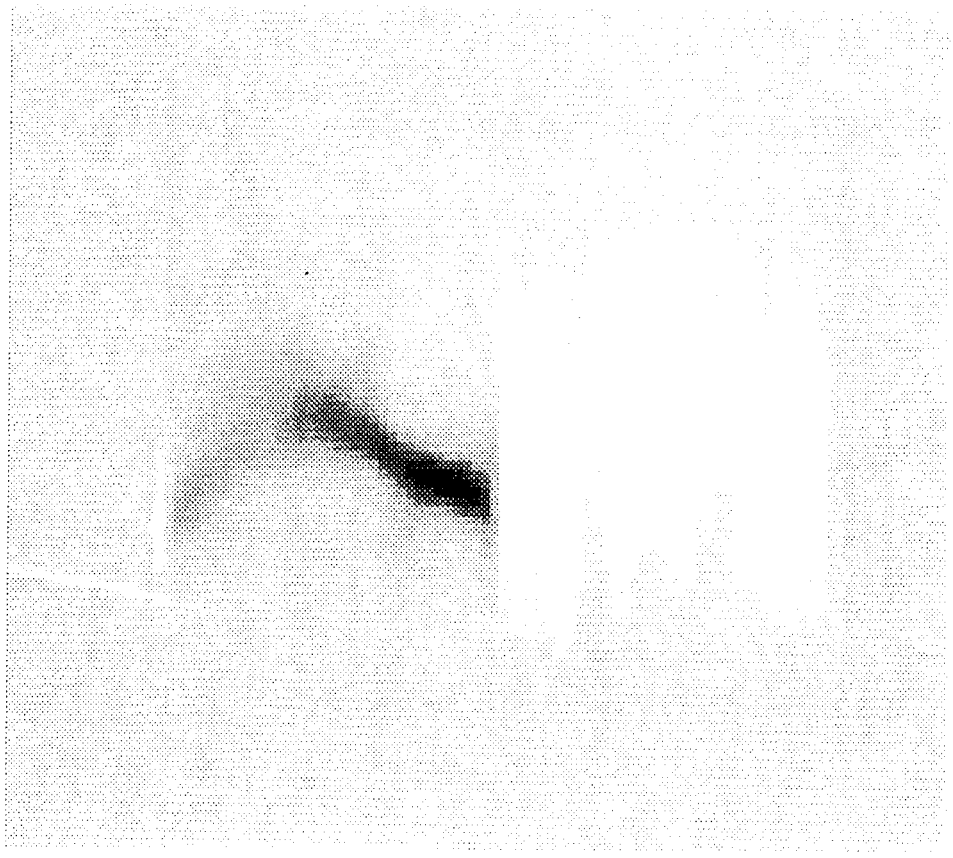

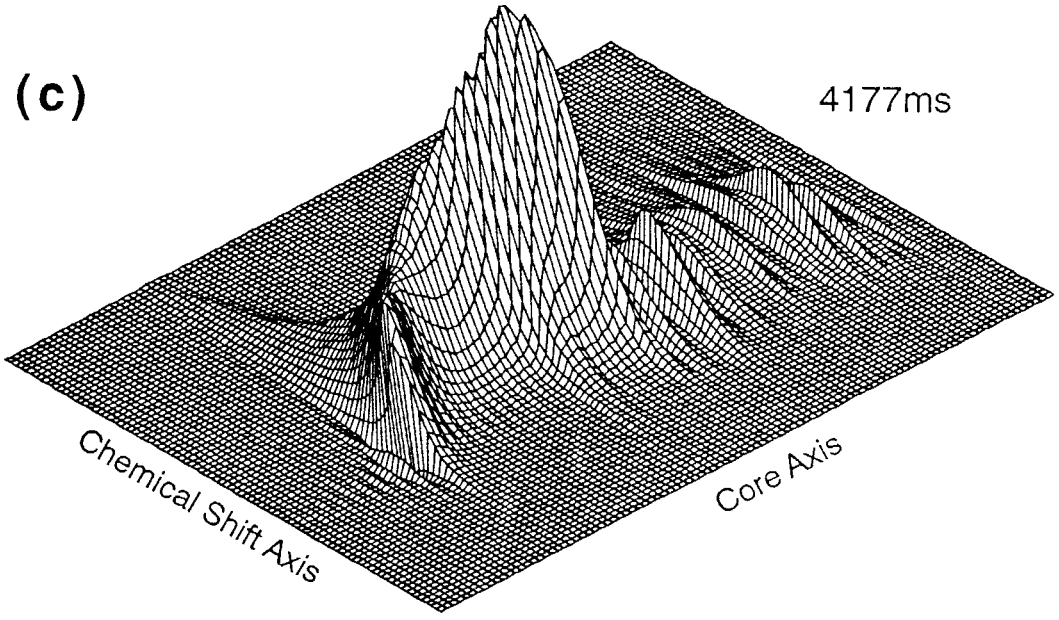
(c)
4177ms
Chemical Shift Axis
Core Axis

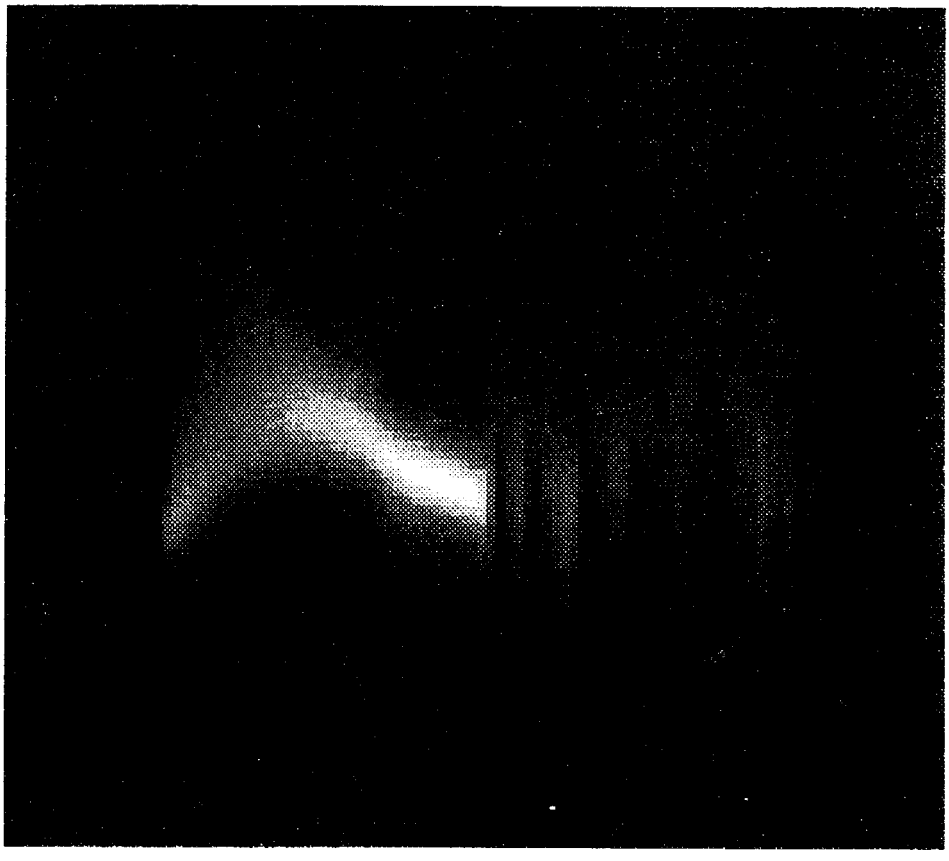

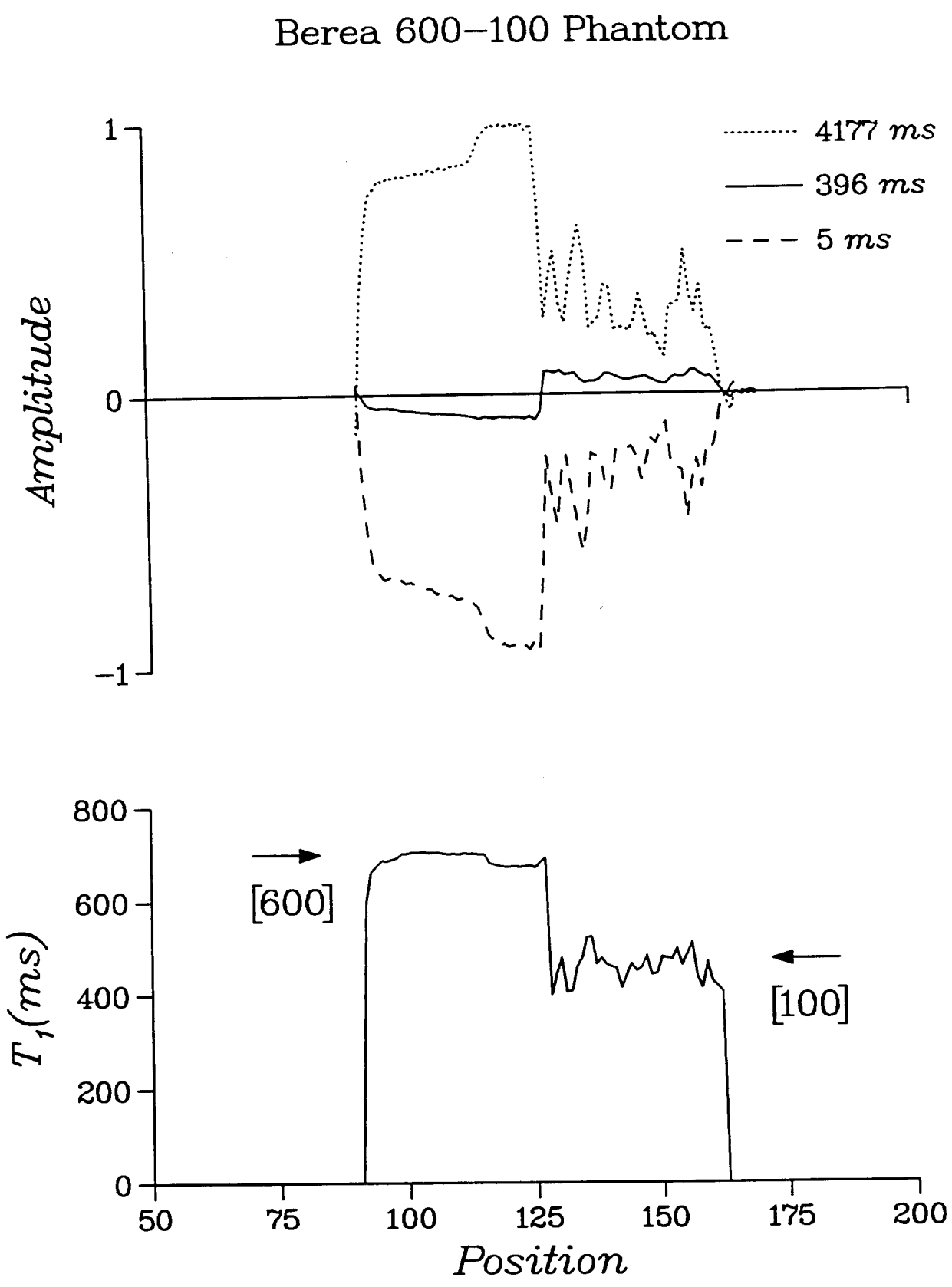

Figure 5. [Upper Panel] Projections obtained by integrating the data displayed in Figure 4 along the chemical shift axis and [Lower Panel] the stretched exponential fit to T_1 are shown as functions of position along the Berea 600-100 phantom core axis.

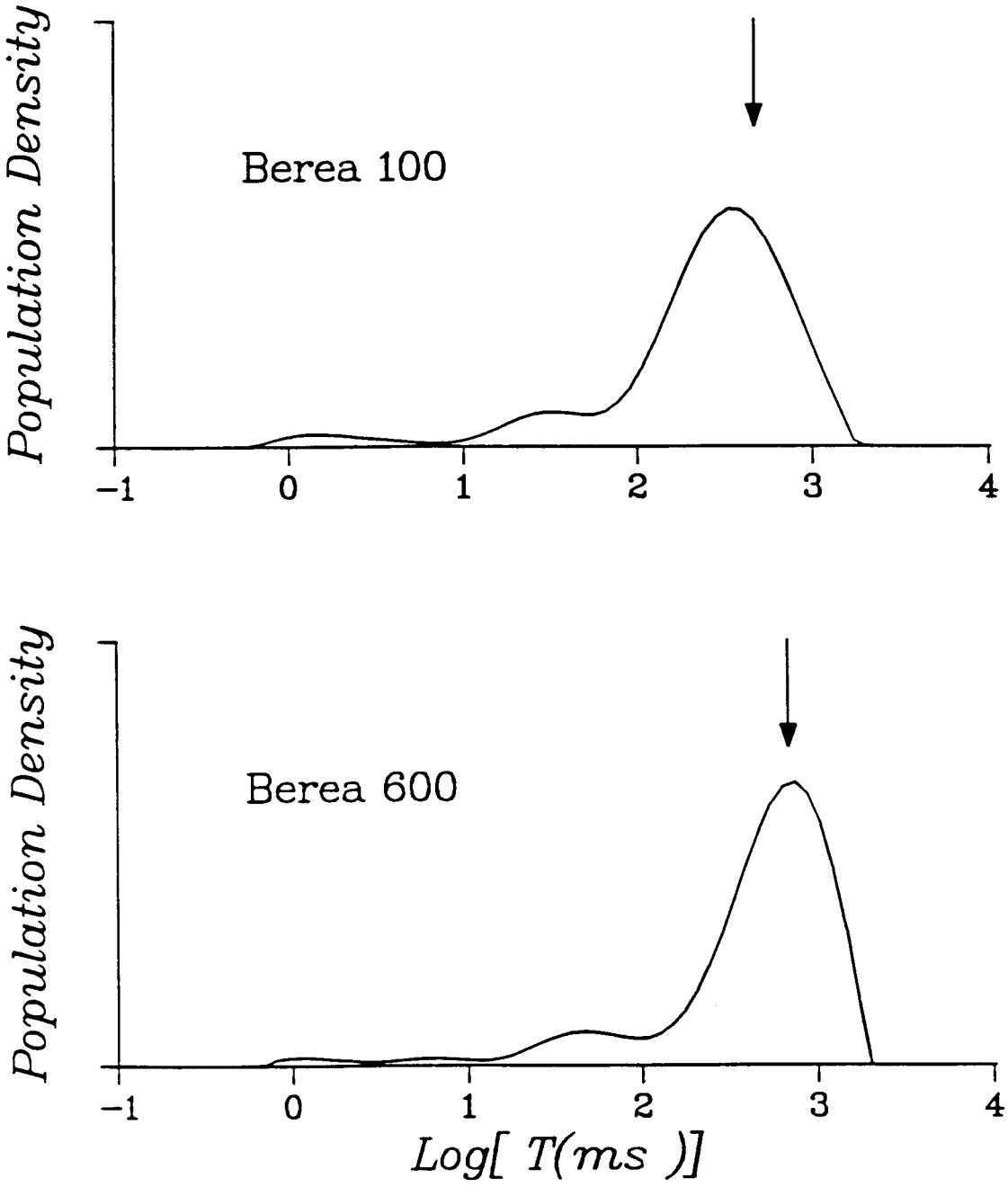

Figure 6. T_1 distributions for Berea 100 and Berea 600 are shown with the positions of the arrows taken from the lower panel of Figure 5 marked. The location of the arrows indicates that the lifetimes measured by our imaging techniques are associated with water in the larger pores.

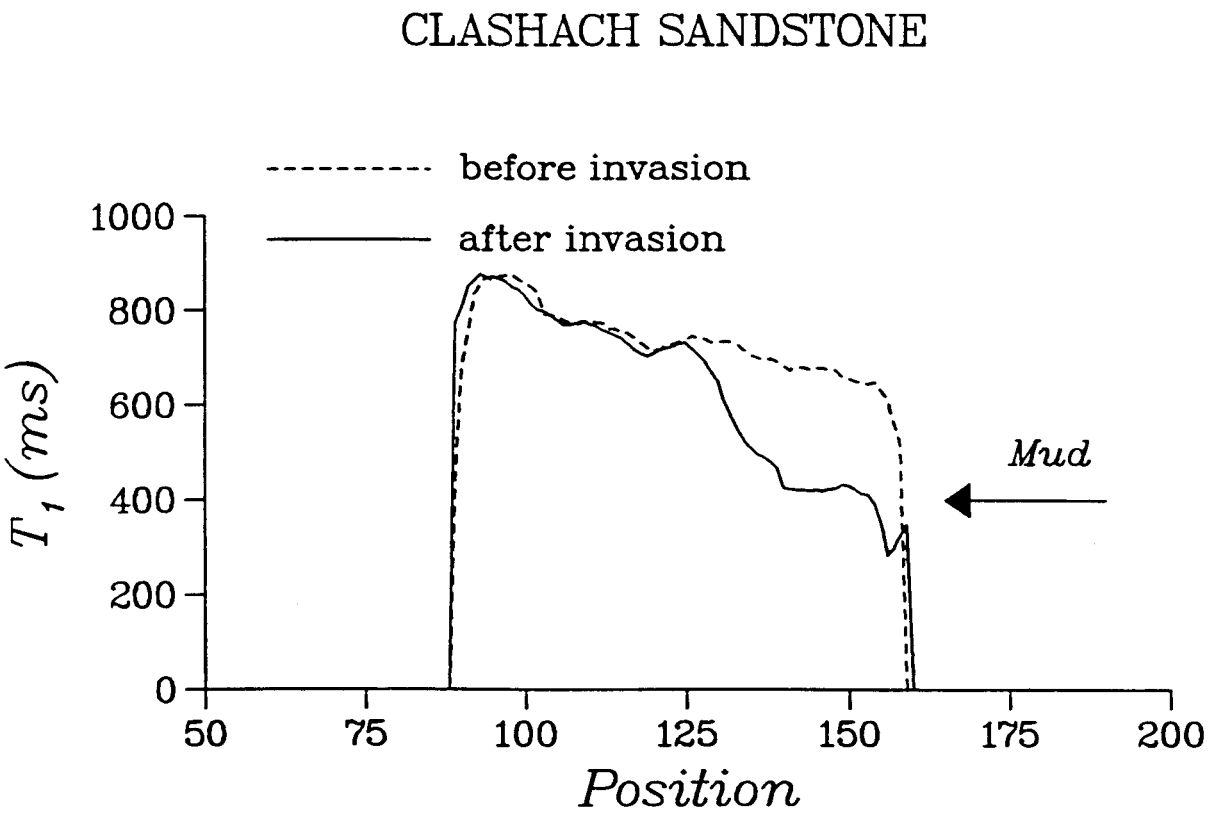

Figure 7. T_1 profiles are shown for a Clashach sandstone core invaded with spud mud.

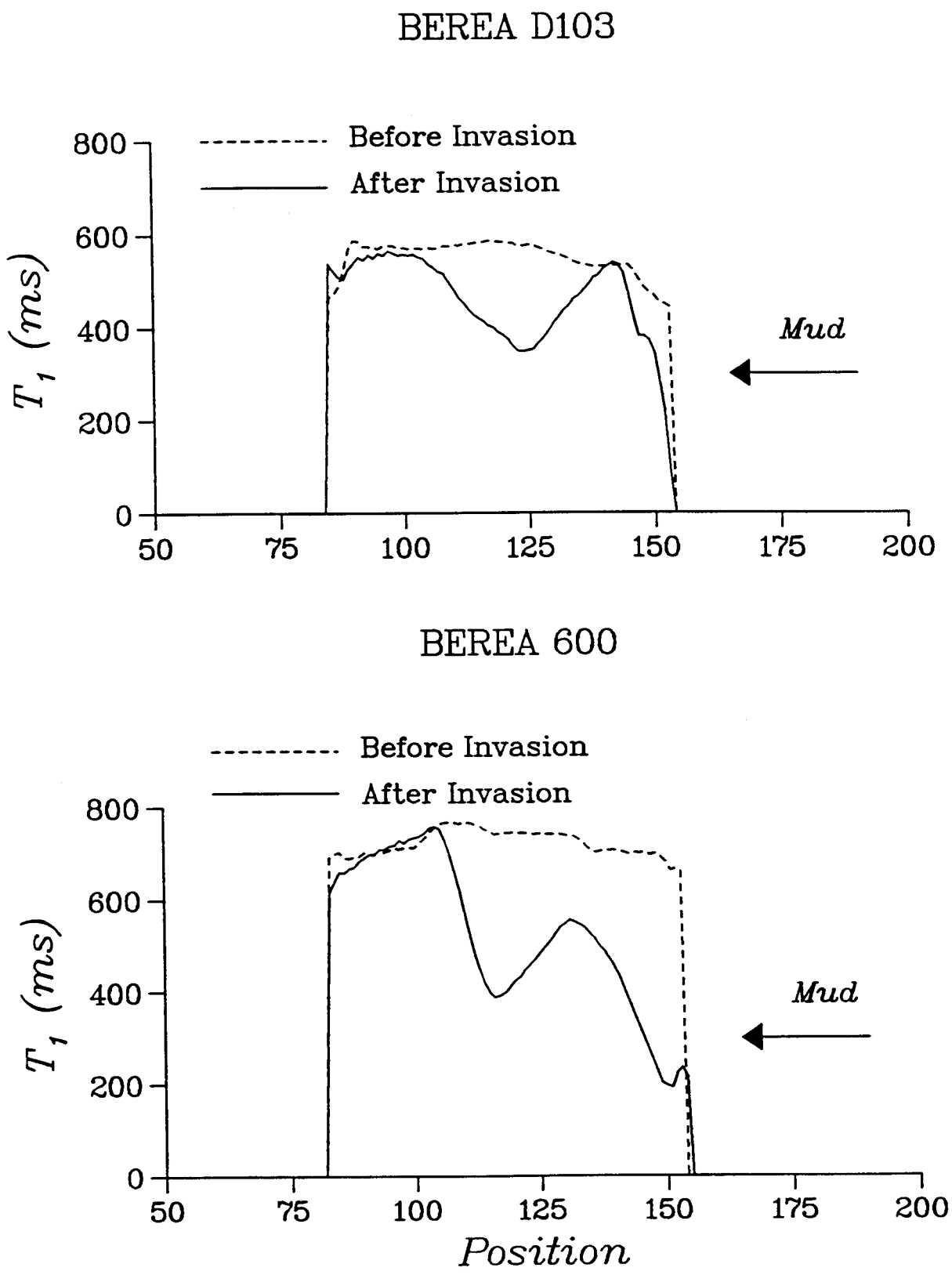

Figure 8. T_1 profiles are shown for Berea 100 and 600 cores invaded with spud mud.

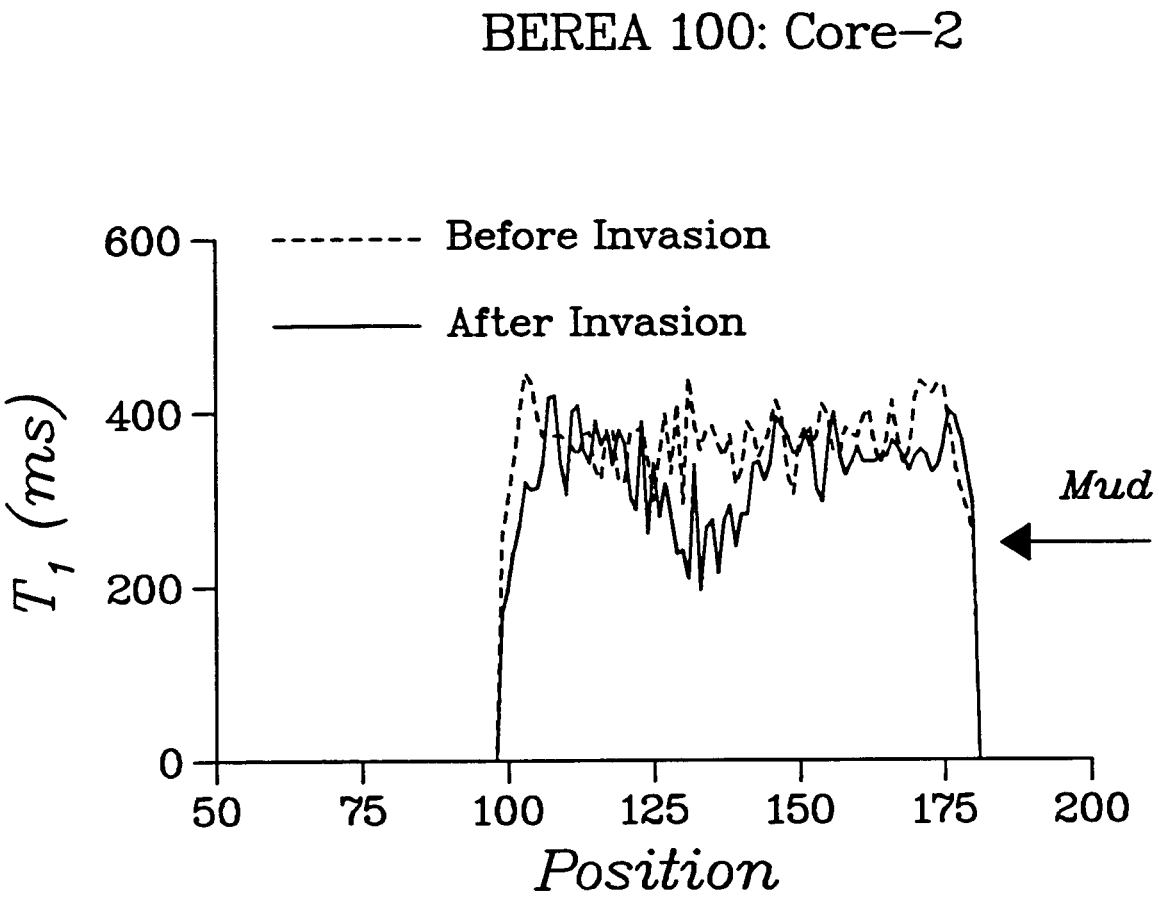

Figure 9. T_1 profiles are shown for a Berea 100 core invaded with a barite weighted bentonite slurry mud.